*energies*

MDPI

*Article*

# Details on the Hydrothermal Characteristics within a Solar-Channel Heat-Exchanger Provided with Staggered T-Shaped Baffles

**Driss Meddah Medjahed [1], Houari Ameur [1], Redha Rebhi [2,3], Mustafa Inc [4,5,6,*], Hijaz Ahmad [7,8,*], Younes Menni [1,*], Giulio Lorenzini [9], Fatimah S. Bayones [10] and Musaad Aldhabani [11]**

1 Department of Technology, University Centre of Naama—Salhi Ahmed, P.O. Box 66, Naama 45000, Algeria; medjahed@cuniv-naama.dz (D.M.M.); ameur@cuniv-naama.dz (H.A.)
2 Department of Mechanical Engineering, Faculty of Technology, University of Medea, Medea 26000, Algeria; rebhi.redha@univ-medea.dz
3 LERM—Renewable Energy and Materials Laboratory, University of Medea, Medea 26000, Algeria
4 Department of Computer Engineering, Biruni University, Istanbul 34025, Turkey
5 Department of Mathematics, Science Faculty, Firat University, Elazig 23119, Turkey
6 Department of Medical Research, China Medical University Hospital, China Medical University, Taichung 40402, Taiwan
7 Section of Mathematics, International Telematic University Uninettuno, Corso Vittorio Emanuele II, 39, 00186 Roma, Italy
8 Mathematics in Applied Sciences and Engineering Research Group, Scientific Research Center, Al-Ayen University, Nasiriyah 64001, Iraq
9 Department of Engineering and Architecture, University of Parma, Parco Area Delle Scienze, 181/A, 43124 Parma, Italy; giulio.lorenzini@unipr.it
10 Department of Mathematics and Statistics, College of Sciences, Taif University, P.O. Box 11099, Taif 21944, Saudi Arabia; f.s.bayones@hotmail.com
11 Department of Mathematics, Faculty of Science, University of Tabuk, P.O. Box 741, Tabuk 71491, Saudi Arabia; maldhabani@ut.edu.sa
* Correspondence: minc@firat.edu.tr (M.I.); hijaz555@gmail.com (H.A.); menni.younes@cuniv-naama.dz (Y.M.)

check for updates

**Citation:** Medjahed, D.M.; Ameur, H.; Rebhi, R.; Inc, M.; Ahmad, H.; Menni, Y.; Lorenzini, G.; Bayones, F.S.; Aldhabani, M. Details on the Hydrothermal Characteristics within a Solar-Channel Heat-Exchanger Provided with Staggered T-Shaped Baffles. *Energies* **2021**, *14*, 6698. https://doi.org/10.3390/en14206698

Academic Editor: Andrej Kitanovski

Received: 9 September 2021
Accepted: 12 October 2021
Published: 15 October 2021



**Abstract:** Details on the hydrothermal characteristics of turbulent flows in a solar channel heat exchanger (CHE) are highlighted. The device has transverse T-shaped vortex generators (VGs). Two staggered VGs (baffles) are inserted on the lower and upper walls of the CHE. The working fluid is Newtonian and incompressible, with constant physical properties. The ANSYS Fluent 17.0 is utilized in this survey. The second-order upwind and QUICK schemes were utilized to perform the discretization of pressure and convective terms, respectively. The SIMPLE algorithm was employed to achieve the speed-pressure coupling. The residual target $10^{-9}$ was selected as a convergence criterion. The effects of the T-VGs' geometrical shape and Reynolds numbers were inspected. At the baffle level, the wall effect was augmented due to the reduction of the passage area of flows, which is estimated here to be 55%, resulting thus in a considerable resistance to the movement of fluid particles. The thermal distribution is highly dependent on the flow structures within the CHE. Since the fluid agitation yields an enhanced mixing, it allows thus an excellent heat transfer. The most considerable rates of thermal transfer were obtained with high Re, which resulted from the intensified mixing of fluid particles through the formation of recirculation cells and the interaction with the walls of the T-VGs and the CHE. The T-baffles with intense flow rates yielded negative turbulent speeds and intensify the fluid agitation, which improves the thermal exchange rates.

**Keywords:** solar channel; heat exchanger; T-baffle; turbulence; heat transfer; hydrothermal; CFD

## 1. Introduction

Thermal devices are utilized in several daily and industrial processes. The optimization of their effectiveness remains of great concern to designers [1–3]. The insertion of

baffles inside the flow duct in HEs is known as an efficient technique to promote the energy performance of such devices [4–6]. The presence of baffles, the so-called vortex generators, yields turbulence and lengthens the fluid particle trajectories, which results in enhanced convective thermal exchange and efficiency [7–9].

Some research studies have been carried out on various types of HEs and their implementations. Patankar et al. [10] produced one of the first numerical studies of hydrothermal activity in a channel heat exchanger with various cross-sections. Kelkar and Ptankar [11] used a parallel-plate channel to insert fins in a staggered pattern. Their numerical simulations for the laminar flow regime revealed that choosing the right geometrical and operational parameters is crucial to improving hydrothermal properties. For low Reynolds numbers (Re), Bazdid-Tehrani and Naderi-Abadi [12] inspected the influence of the blockage ratio (BR) on the hydrothermal fields within a 2D horizontal CHE provided with in-line ribs. The VGs in the shape of ribs are not highly efficient for high amounts of BR, as claimed by these authors. Compared with a smooth backward-facing step, Tsay et al. [13] observed an augmentation in Nusselt number (Nu) by 190% with the presence of a vertical baffle on the bottom wall of the step. Great dependence on the hydrothermal features according to the position of the baffle inside the step was observed.

Pirouz et al. [14] analyzed the influence of adding two staggered baffles on the lower and upper walls of a duct. The Lattice Boltzmann Method (LBM) was confirmed to be accurate and efficient for predicting the conjugate thermal transfer phenomena. Additionally, Nasiruddin and Siddiqui [15] considered three baffle orientations in a tube heat exchanger, namely: vertical and inclined towards the upstream and the downstream ends. The inclination of baffles towards the downstream end yielded less pressure drop with similar heat transfer rates, compared with the other cases. Furthermore, Demartini et al. [16] examined the aerothermal details of air flowing through a CHE equipped with two baffles on the lower and upper walls. Moreover, Gajusingh et al. [17] used the PIV (Particle Image Velocimetry) technique to explore the impact of VGs on the thermal phenomenon within a smooth pipe. Compared with the smooth pipe, the VG induced enhancement in the turbulent velocities by three times and a significant increase in energy production rates. The biggest improvement in the turbulence magnitude was reached in the area within a distance of two heights of the VG from the lower wall just downstream of the VG. Other related achievements are available in the literature like Sakhri et al. [18–20], Chamkha and Menni [21], Boursas et al. [22], Chekchek et al. [23], Hadidi et al. [24], and Menni et al. [25]. Also, Salmi et al. [26] tried to enhance the convective heat transfer in CHE baffles with vortex generators. Additionally, Dutta and Hossain [27] inspected the impact of various geometrical parameters and Reynolds numbers of the thermal transfer and pressure losses inside a CHE provided with perforated and inclined baffles. Aiming to eliminate or to reduce the poor heat transfer areas (PHTAs) that are created in the downstream region of baffles, Sahel et al. [28] introduced a row of four holes at various locations. These locations are known as the pore axis ratio (PAR). In comparison with the simple baffle, the highest thermal efficiency of 64%, as well as the lowest reduction in pressure drop of 12 times, were obtained with PAR = 0.190.

Other researchers have been interested in the baffling technique by using porous material baffles. Among other studies, Yang and Hwang [29], Yilmaz [30], and Guerroudj and Kahalerras [31] found a significant relationship of hydrothermal features on the assigned baffle porosity and duct aspect ratio. The baffle shape is another significant issue in the design and performance of thermal devices. Many shapes have been proposed and analyzed, like diamond [32], helical and continuous [33], twisted [34], delta [35], trapezoidal winglet [36], arc [37], trisection helical [38], oblique horseshoe [39], 'U' [40], 'V' [41,42], perforated 'V' [43], double 'V' [44], discrete 'W' [45], and 'Z'-shaped [46].

In the present work, a newly designed shape of the baffle was considered. It concerns T-shaped baffles inserted in a horizontal CHE with a constant temperature on the duct walls. The turbulent airflow patterns and thermal fields were predicted numerically under various operating conditions.

## 2. Problem under Inspection

The physical model is schematically highlighted in Figure 1, where the geometrical characteristics are similar to the experimental work in Ref. [16]. A horizontal duct with two transverse T-shaped obstacles inserted on the top and bottom surfaces of the exchanger was employed. The length L, width (W), and height (h) of the duct were 0.554, 0.193, and 0.146 m, respectively. Baffle No. 1 was inserted on the upper surface at $L_{in}$ = 0.218 m from the channel inlet. The clearance between the two baffles was c = 0.142. The baffle height was a = 0.08 m, which corresponds to a reduced space of the flow passage at the baffle level by 54.79%. The thickness of the T-shape was b = 0.01 m. A constant temperature ($T_w$ = 375 K) was set on the top and bottom surfaces of the CHE. A uniform temperature ($T_{in}$ = 300 K) and constant velocity profile of the fluid (u = $U_{in}$, v = 0) with 2% of turbulence intensity were defined at the inlet section of the duct.

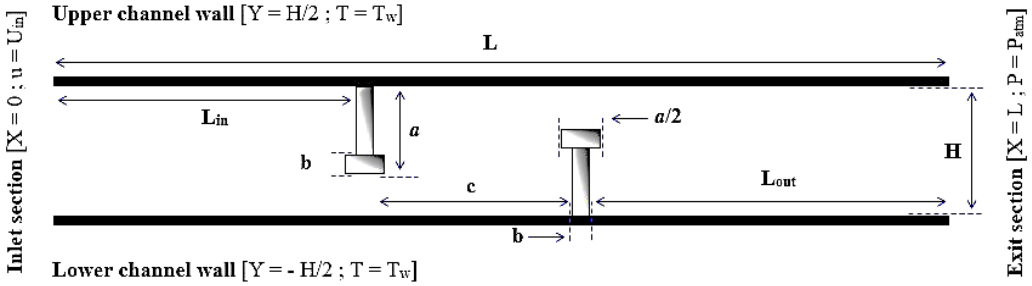


**Figure 1.** Channel heat exchanger with T-shaped baffles.

For air fluidity (Prandtl number Pr = 0.71), the Reynolds numbers ranged within 12,000–32,000. No-slip and impermeable boundary conditions were put for the walls of the channel and baffles. P = $P_{atm}$ was put at the exchanger exit.

## 3. Mathematical Tools

### *3.1. Considerations*

The study was carried out by the CFD method, where the following considerations were undertaken during the computations: two-dimensional, turbulent, and steady-state flow, for a Newtonian and incompressible fluid. The thermal transfer by radiation and viscous dissipation were neglected. The main equations were:

$$\frac{\partial}{\partial x_i}(\rho u_i) = 0 \tag{1}$$

$$\frac{\partial}{\partial x_i}(\rho u_i u_j) = \frac{\partial}{\rho x_i}\left[\mu\left(\frac{\partial u_i}{\partial x_j} - \rho\overline{u_i' u_j'}\right)\right] - \frac{\partial P}{\partial x_i} \tag{2}$$

where P, $\rho$, and $\mu$ are the pressure, fluid density, dynamic viscosity. $u_i$ and $u_j$ are mean velocity components in $x_i$ and $x_j$ directions.

$$\frac{\partial}{\partial x_i}(\rho u_i T) = \frac{\partial}{\rho x_i}\left((\Gamma + \Gamma_t)\frac{\partial T}{\partial x_j}\right) \tag{3}$$

where $\Gamma_t$ and $\Gamma$ are, respectively, the turbulent thermal diffusivity and molecular thermal diffusivity, defined as:

$$\Gamma = \mu/\mathrm{Pr} \quad \text{and} \quad \Gamma_t = \mu_t/\mathrm{Pr}_t \tag{4}$$

In Equation (2), $\rho\overline{u_i' u_j'}$ is the Reynolds stresses defined by the Boussinesq hypothesis as:

$$-\rho\overline{u_i' u_j'} = \mu_t\left(\frac{\partial u_i}{x_j} + \frac{u_j}{x_i}\right) - \frac{2}{3}\left(\rho k + \mu_t\frac{\partial u_i}{\partial x_j}\right)\delta_{ij} \tag{5}$$

where $\delta_{ij}$ is the Kroenecker delta and $\mu_t$ the eddy viscosity defined as:

$$\mu_t = \rho C_\mu \frac{k^2}{\varepsilon} \tag{6}$$

*3.2. Turbulence Model*

The standard k-ε model was utilized. It is defined by.

3.2.1. k-Equation

It is represented as follows:

$$\frac{\partial}{\partial x_j}(\rho k u_j) = \frac{\partial}{\partial x_j}\left[\left(\mu + \frac{\mu_t}{\sigma_k}\right)\frac{\partial k}{\partial x_j}\right] + G_k + \rho\varepsilon \tag{7}$$

3.2.2. ε-Equation

It is defined as:

$$\frac{\partial}{\partial x_j}(\rho \varepsilon u_j) = \frac{\partial}{\partial x_j}\left[\left(\mu + \frac{\mu_t}{\sigma_\varepsilon}\right)\frac{\partial \varepsilon}{\partial x_j}\right] + C_{1\varepsilon}\frac{\varepsilon}{k} - C_{2\varepsilon}\rho\frac{\varepsilon^2}{k} \tag{8}$$

where

$$C_\mu = 0.99; \quad C_{1\varepsilon} = 1.44; \quad C_{2\varepsilon} = 1.92; \quad \sigma_k = 1.0; \quad \sigma_\varepsilon = 1.3 \tag{9}$$

are the empirical constants of the model.

*3.3. Governing Parameters*

3.3.1. Reynolds Number

It is calculated as:

$$\mathrm{Re} = \rho \overline{U} D_h / \mu \tag{10}$$

where $D_h$ is the hydraulic diameter, given by:

$$D_h = 2HW/(H+W) \tag{11}$$

3.3.2. Friction Factor

It is given by:

$$f = \frac{(\Delta P/L)D_h}{\frac{1}{2}\rho \overline{U}^2} \tag{12}$$

where $\overline{U}$ is the average axial velocity, and $\tau_w$ is the shear stress.

3.3.3. Heat Transfer

The local ($Nu_x$) and average (Nu) Nusselt numbers are:

$$Nu_x = \frac{h_x D_h}{k_f} \tag{13}$$

$$Nu = \frac{1}{L}\int Nu_x \partial x \tag{14}$$

*3.4. Experimental Correlations*

To normalize the values of f and Nu, the Petukhov [47] and Dittus–Boelter [48] correlations (Equations (15) and (16), respectively) can be used. The quantities $f_0$ and $Nu_0$ are the friction factor and the average Nu for an unbaffled channel, respectively.

3.4.1. Petukhov Correlation

It is calculated by:

$$f_0 = (0.79 \ln \mathrm{Re} - 1.64)^{-2} \text{ for } 3 \times 10^3 \leq \mathrm{Re} \leq 5 \times 10^6 \quad (15)$$

3.4.2. Dittus–Boelter Correlation

It is defined as:

$$Nu_0 = 0.023 \mathrm{Re}^{0.8} \mathrm{Pr}^{0.4} \text{ for } \mathrm{Re} \geq 10^4 \quad (16)$$

*3.5. Thermal Enhancement Factor (TEF)*

It is given by:

$$TEF = (Nu/Nu_0)/(f/f_0)^{1/3} \quad (17)$$

## 4. Computational Details

*4.1. Numerical Methods*

In this survey, ANSYS Fluent 17.0 was used. The discretization of pressure and convective terms was done using the second-order upwind and QUICK methods, respectively [49,50]. To accomplish the speed-pressure coupling, the SIMPLE algorithm was adopted. As a convergence criterion, the residual goal $10^{-9}$ was selected.

*4.2. Mesh Dependency Tests*

The computational domain was created by GAMBIT. To control the flow changes near the wall, the mesh was refined near the walls of the channel and baffles. Mesh sizes were varying in the ranges of 95–370 and 35–145 for the length and depth of the duct. The results depicted in Table 1 show a small variation in Nu values (less than 0.35%) with the mesh 245 × 95. This mesh size was utilized in all computations.

**Table 1.** Influence of mesh size on Nu, at Re = $8.73 \times 10^4$.

| **Mesh** | 95 × 35 | 120 × 45 | 145 × 55 | 170 × 65 | 195 × 75 | 220 × 85 | 245 × 95 | 370 × 1145 (reference) |
|---|---|---|---|---|---|---|---|---|
| **Nu** | 210.56 | 212.128 | 214.592 | 218.624 | 219.52 | 222.096 | 223.216 | 224 |

*4.3. Validation of the Model*

The validation of some computed findings was performed against those in Ref. [16]. With similar geometric conditions as these authors, the variation of axial velocity is depicted in Figure 2a,b. At Re = $8.73 \times 10^4$ and x = 0.525 m, the velocity curves are presented along with the duct depth. As shown, a satisfactory agreement was found from the comparison between both results.

Another verification of the predicted results of the Nusselt number ($Nu_0$) was performed against the correlation of Dittus–Boelter [48] for a smooth duct (Figure 3). The correlation that is given in Equation (16) was applied for a range of Re of 12,000 to 32,000. The second verification revealed a deviation from the correlation results by 3.5%, which confirms the reliability of our numerical model.

On the other hand, many other studies, such as Menni et al. [41,42,51,52], have investigated numerically the same CHE in the presence of other different VGs. All of these studies adopted the same numerical methods, the range of mesh density in both X and Y axes, as well as the validity of the numerical model.

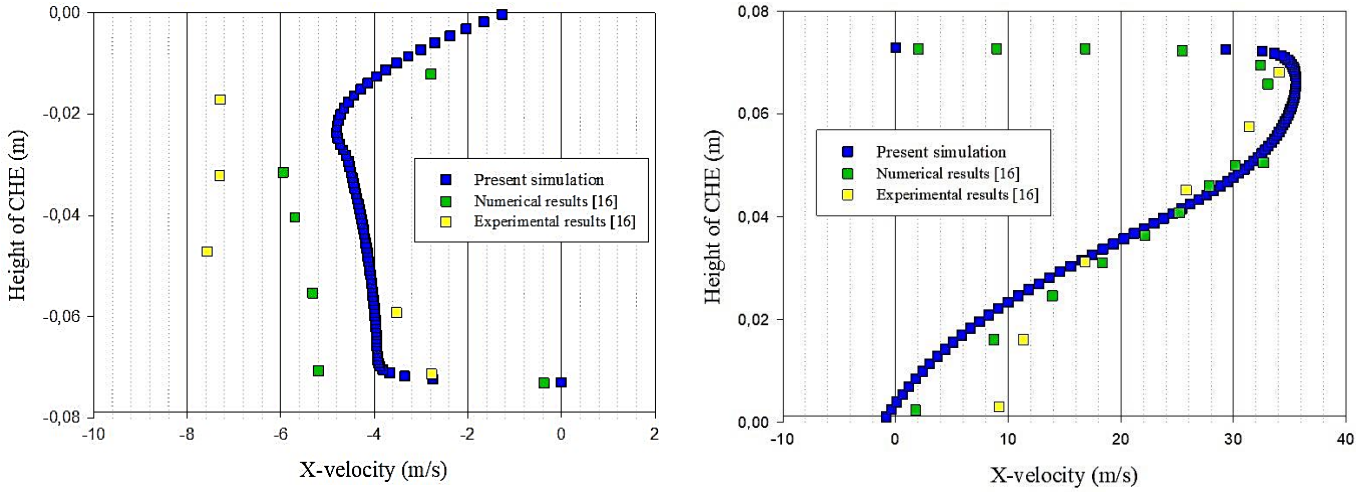


**Figure 2.** Axial velocity curves at Re = 8.73 × $10^4$ and x = 0.525 m: Validation against experimental data. (**a**) Lower side of the CHE. (**b**) Upper side of the CHE.

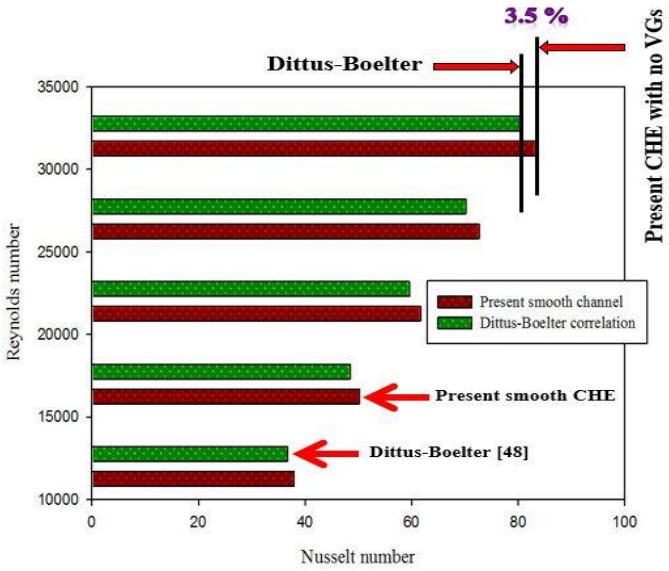


**Figure 3.** Nu values for an unbaffled duct.

## 5. Findings and Analysis

From the five plots of flow fields highlighted in Figure 4, three main zones are distinguished. In the first one, a particle fluid acceleration with great axial velocity is observed just upstream of the baffles, where the streamlines are deflected. Another acceleration of fluid flow is yielded in the area limited by the obstacle tip and the channel surface (i.e., 2nd zone), which is due to the limitation of the main passage area of flows. In the region following the baffles (i.e., 3rd zone), the expansion impact on the flow patterns is significant, where the recirculation cells extend with the raise of Re.

The variation of the mean velocity along the channel domain is highlighted in Figure 5. Low velocities of fluid flow are observed in recirculation loops that are formed around the baffles, and precisely in the corner zones. In the regions elsewhere, the flow is reattached, and the streamlines become uniform and parallel. The sudden variation of the flow direction that is caused by the first baffle yields an increase in speed in the area between the baffle tip and the duct wall.

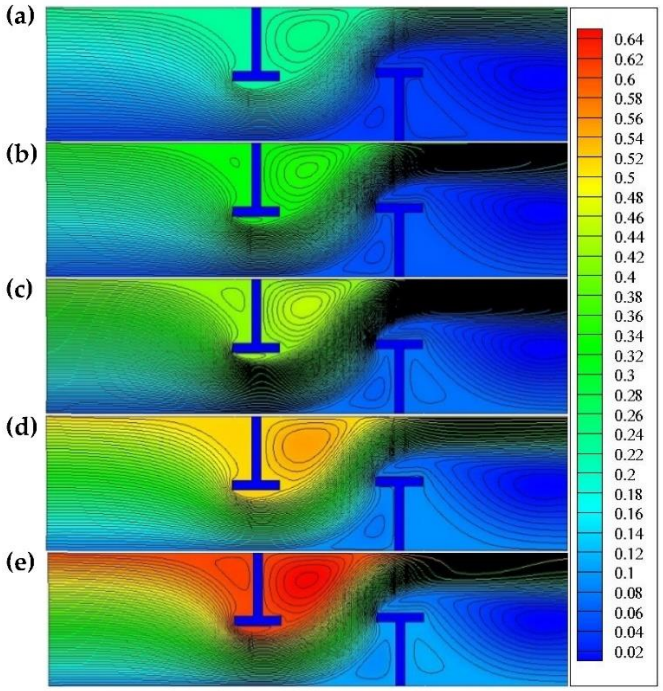


**Figure 4.** Flow patterns for: Re = (**a**) 12,000; (**b**) 17,000; (**c**) 22,000; (**d**) 27,000; (**e**) 32,000.

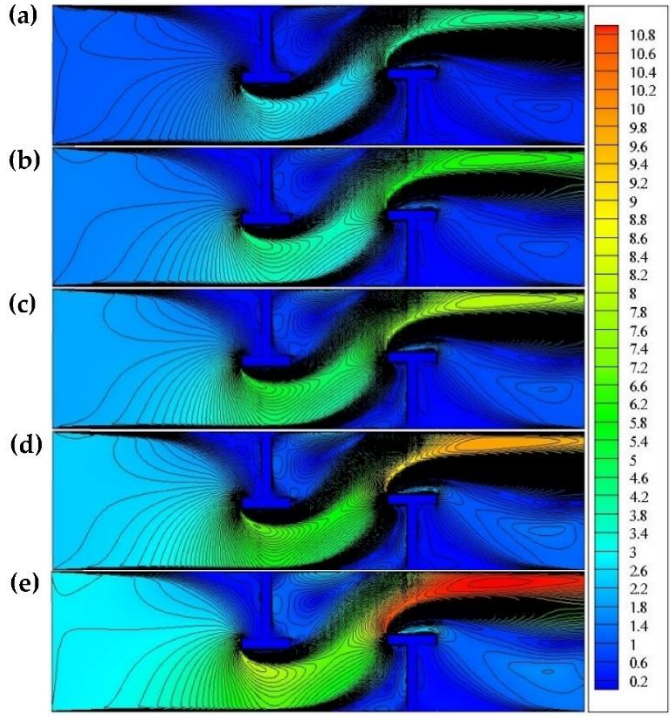


**Figure 5.** Velocity distribution for: Re = (**a**) 12,000; (**b**) 17,000; (**c**) 22,000; (**d**) 27,000; (**e**) 32,000.

Besides this, the most significant amounts of velocity, by about 406.54% over $U_{in}$, are observed near the upper wall of the duct just behind the second VG. Moreover, a proportional increase in the velocity is remarked with the raise of Re for the geometrical case under investigation. Variations of the air transverse speed are depicted in Figure 6. The speed gradients are negative and then positive at the tip of the first and second baffle tips, respectively. The most significant amounts of velocity are observed in the left corner of the first baffle and they become more considerable with increased Re.

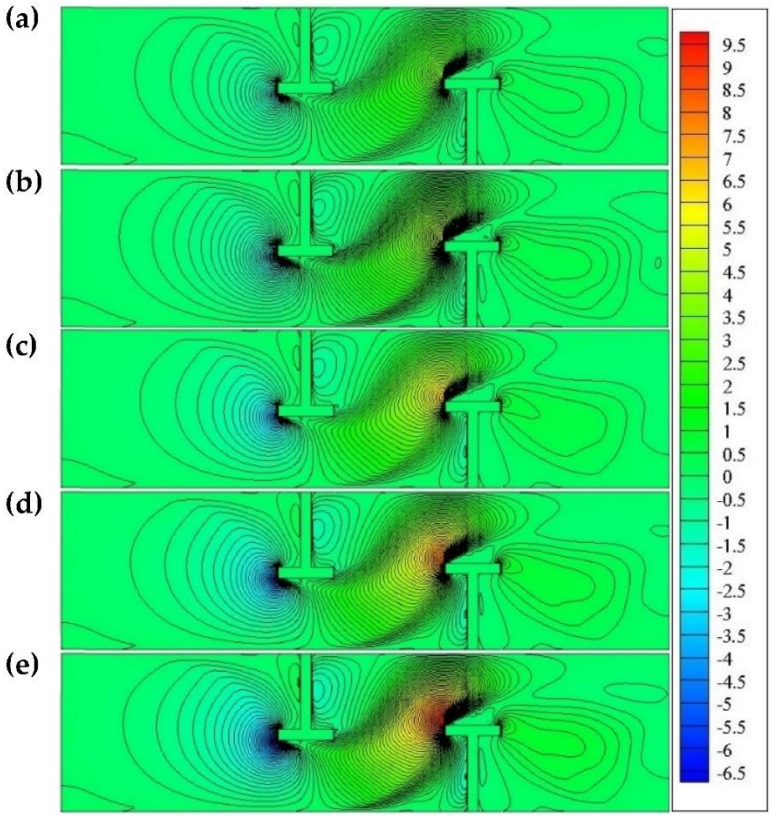


**Figure 6.** Fields of Y-velocity for: Re = (**a**) 12,000; (**b**) 17,000; (**c**) 22,000; (**d**) 27,000; (**e**) 32,000.

Changes in the dynamic pressure (P) are also highlighted under two-dimensional plots along with the exchanger, as seen in Figure 7. The same distribution as that of the velocity (reported in Figure 5) is observed. In general, the most significant values of the dynamic pressure are located in regions where the flow velocities are intense. The lower amounts of pressure are located in the vicinity of baffles and precisely behind them due to the existence of vortices. However, the highest values of P are obtained on the inner wall of the exchanger, in the region of the front to the baffles tip. Additionally, the raise of Re yields a continuous increase in P amounts.

Another critical parameter is inspected and presented in Figure 8. It concerns turbulent kinetic energy (TKE), where its variation is given according to various Re. The amounts of TKE are varying from negligible at low Re in almost all the ducts, to feeble at moderate Re in the area from the 1st VG to the duct exit, until it becomes significant at high Re. Limited amounts of TKE are recorded on the walls of the 1st VG and the left corner of the 2nd one. The intensification of Re values generates a raise in the TKE, where several loops are formed above the tip of the 2nd VG and near the upper surface of the device. At the baffle level, the wall effect is augmented due to the reduction of the passage area of flows, which is estimated here to be 55%, resulting thus in a considerable resistance to the movement of fluid particles.

Changes in the turbulent dissipation rates (TDR) are also examined for several Re values (Figure 9). Three main regions are distinguished. The first one corresponds to the position of the 1st VG, where the flow paths are sharply destroyed, resulting thus in augmented friction. The 2nd region concerns the area near the 2nd VG, from the lower corner and through the left side of VG, towards the duct outlet. The 3rd region is the area above the 2nd VG next to the upper surface of the device. The 3rd region is also characterized by significant values in friction due to the strong variation in flow patterns, as well as the interaction with the exchanger walls. Furthermore, and as expected, an augmentation of TDR values is induced with the raise of Re, especially in the upper part of the 2nd VG.

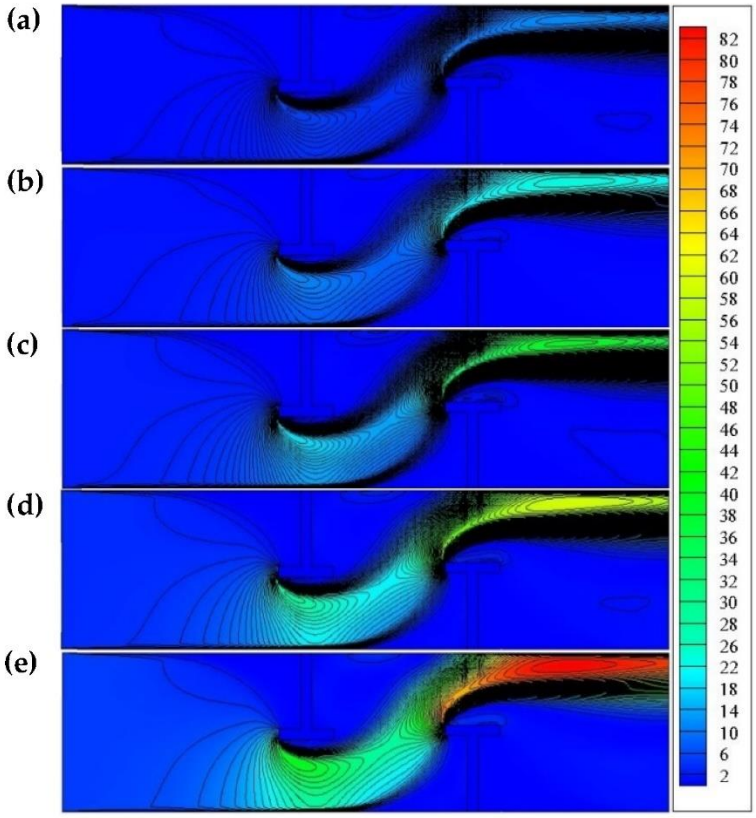


**Figure 7.** Distribution of the dynamic pressure for: Re = (**a**) 12,000; (**b**) 17,000; (**c**) 22,000; (**d**) 27,000; (**e**) 32,000.

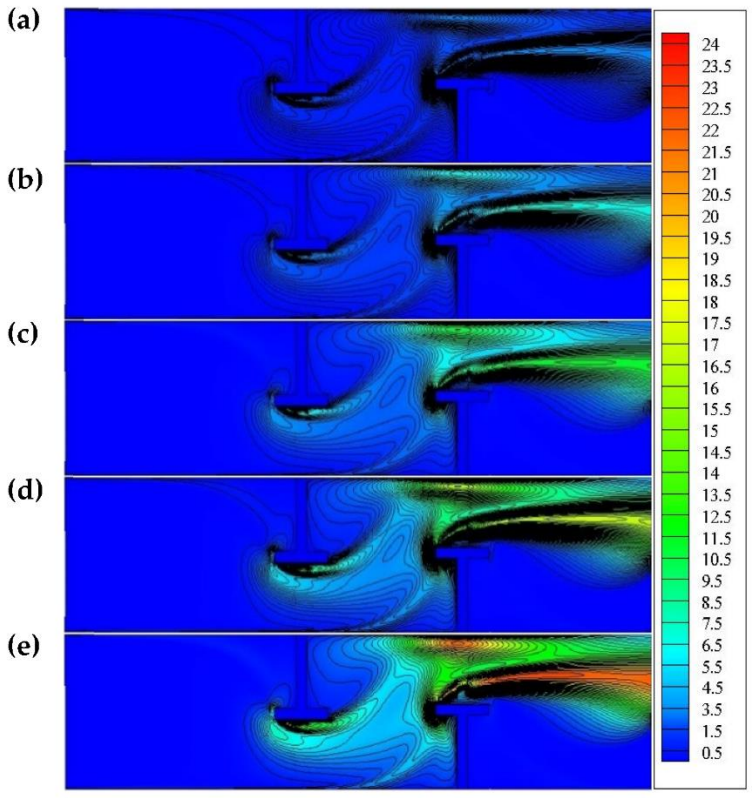


**Figure 8.** Variation of the turbulent kinetic energy for: Re = (**a**) 12,000; (**b**) 17,000; (**c**) 22,000; (**d**) 27,000; (**e**) 32,000.

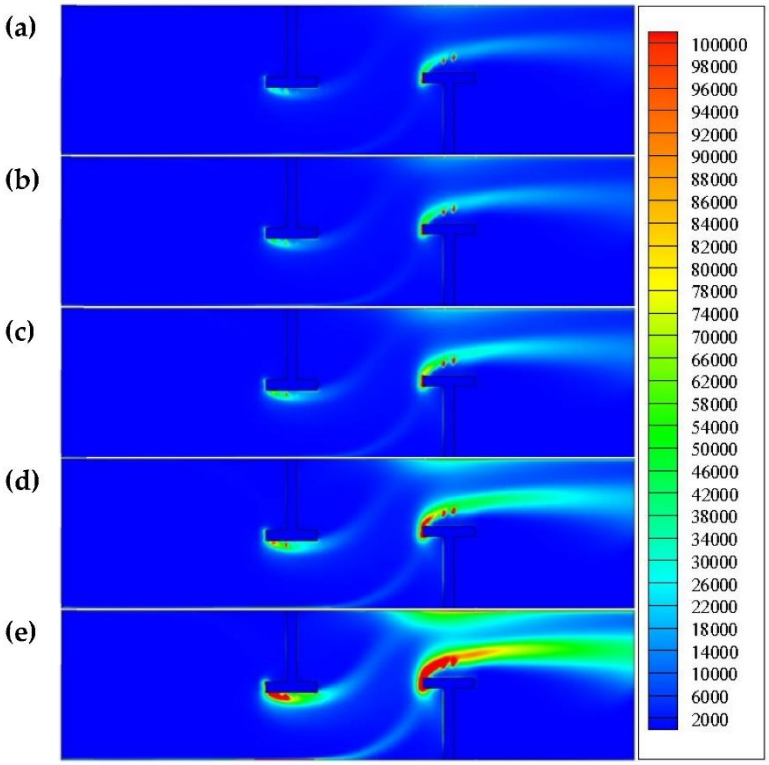


**Figure 9.** Fields of the turbulent dissipation rates for: Re = (**a**) 12,000; (**b**) 17,000; (**c**) 22,000; (**d**) 27,000; (**e**) 32,000.

The effects of Reynolds numbers on the turbulent intensity (TI) are also examined (Figure 10). As highlighted, a rapid and ample increase in the TI amounts is yielded with increasing Re, compared with those of TKE (Figure 8). The gradual augmentation of TI begins from the 1st VG, while marginal amounts are obtained at the 2nd VG next to the top surface of the exchanger.

The thermal behavior within the CHE equipped with T-vortex generators (T-VGs) is inspected in Figure 11. The thermal distribution is highly dependent on the flow structures within the CHE. Since the fluid agitation yields an enhanced mixing, it allows thus an excellent heat transfer.

The thermal distribution reported in Figure 11 reveals a drop in the temperature magnitude in the area between the obstacles end and the opposing wall of the exchanger. The heat transfer process starts just after the 1st VG. Furthermore, and compared with the unbaffled CHE, high amounts of the temperature are observed in the recirculation cells that are formed in the area downstream of the T-VGs. In this region, a poor heat transfer process is occurring. Additionally, an inverse proportionality is remarked between T and Re, where a significant temperature drop is induced with increasing Re (Figure 11).

The impact of the T-shaped model of vortex generators on the profiles of axial velocity (U) is inspected for various locations within the channel (Figure 12). The 1st baffle yields a dead zone at its right corner and low velocities in the upper half of the device, where Velocities with negative values represent the existence of recirculating cells. These negative velocities are present at each corner of the T-baffle, as seen in Figure 12a,b.

At x = 0.255 and 0.285 m, i.e., in the downstream region of the upper T-baffles, two wide areas are distinguished (Figures 12c and 12d, respectively). The 1st area is that where the air particles follow the principal direction of the stream and the U-profiles are still parabolic. The 2nd vortex loop is located in the right corner of the T-VG, where the U-curves are oriented towards the opposite direction of the stream. The U-profiles in the space between the two T-fins are plotted in Figures 12e and 12f for x = 0.315 and 0.345 m, respectively.

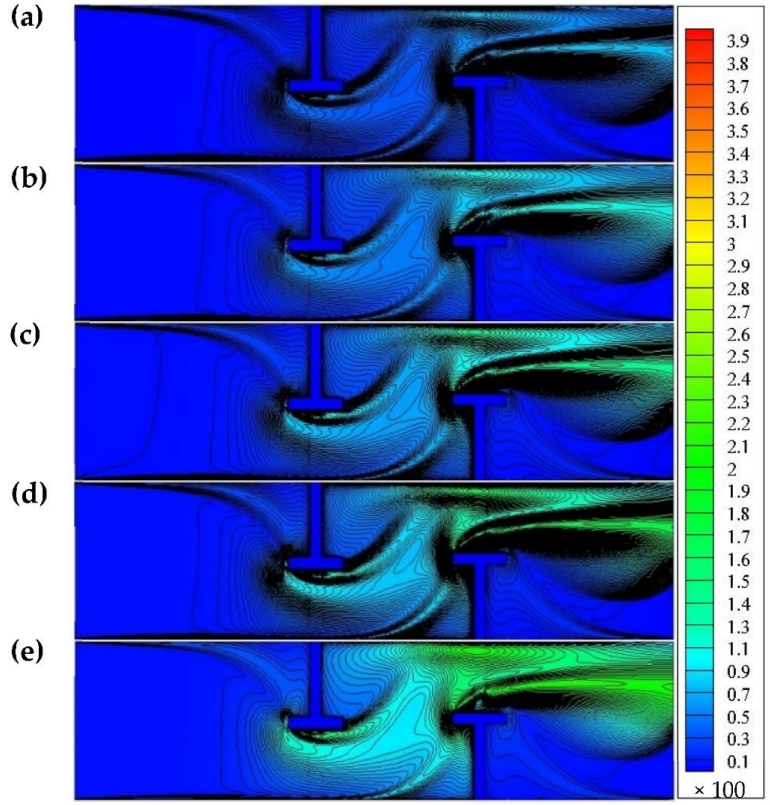


**Figure 10.** Turbulent intensity vs. flow rate: Re = (**a**) 12,000; (**b**) 17,000; (**c**) 22,000; (**d**) 27,000; (**e**) 32,000.

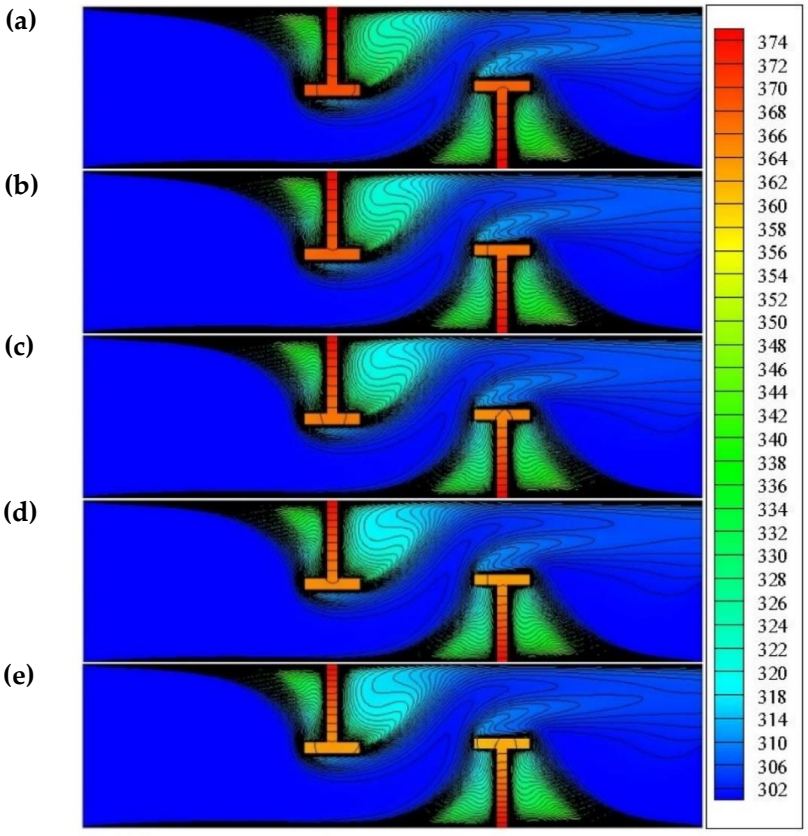


**Figure 11.** Impact of Re on the thermal fields: Re = (**a**) 12,000; (**b**) 17,000; (**c**) 22,000; (**d**) 27,000; (**e**) 32,000.

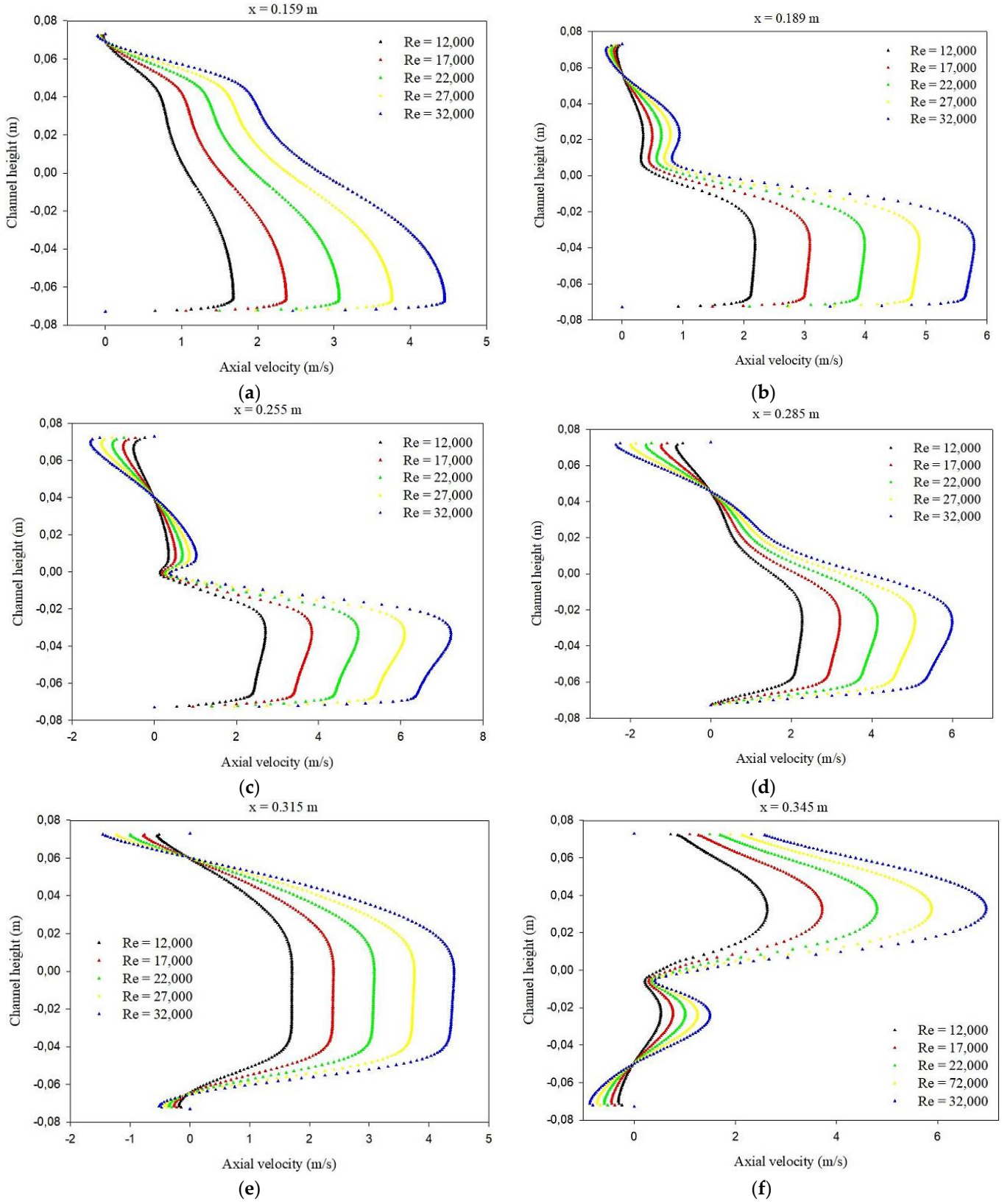


**Figure 12.** *Cont.*

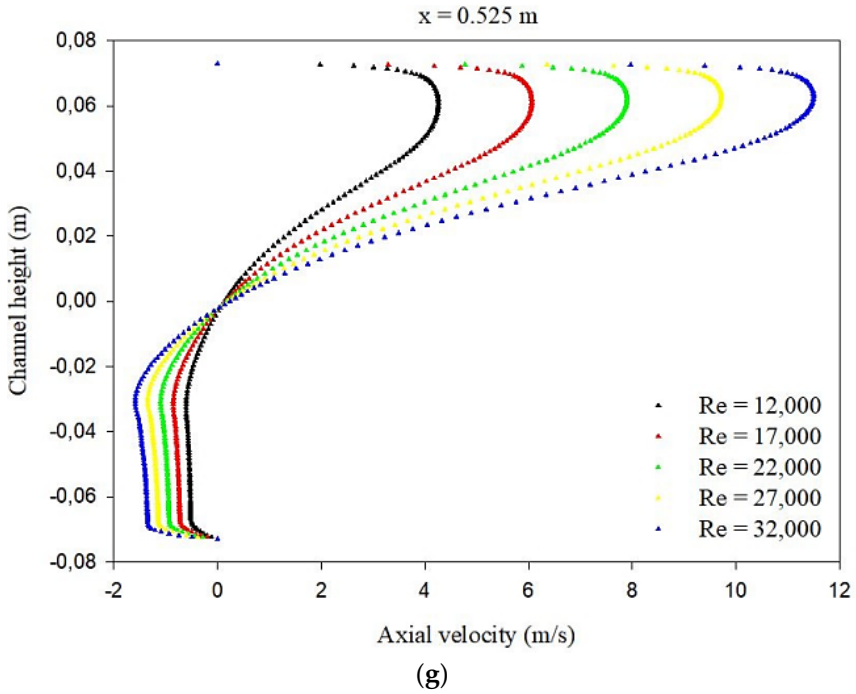


(**g**)

**Figure 12.** Changes in the axial velocity vs. Re for several locations within the channel: (**a**) x = 0.159 m; (**b**) x = 0.189 m; (**c**) x = 0.255 m; (**d**) x = 0.285 m; (**e**) x = 0.315 m; (**f**) x = 0.345 m; (**g**) x = 0.525 m.

When approaching the 2nd VG, the velocity decreased in the lower half of the duct, whereas a new acceleration of the flow started from the tip of this obstacle. Additionally, the 2nd T-shaped VG generates a considerable movement of the fluid particles in the vertical direction, which increases the reattachment length of the separated flows. At the location, x = 0.525 m from the inlet section, i.e., at 0.145 m after the 2nd T-VG, the velocity reaches the value 11.496 m/s, which is higher by about 4.120 times than that at the inlet (Figure 12g). This is generated by the strong interaction of the fluid particles with the wall of the 2nd T-baffle. Moreover, and as illustrated in the plots of Figure 12, the size of the recirculation loops, as well as the reattachment length, augments with the raise of Re.

The T-baffles revealed a similar behavior to the above with a sudden expansion, which induces vortices in the vertical direction relative to the horizontal plane of the channel. From its definition, the heat transfer coefficient does not allow a local determination of regions where poor heat transfer occurs. From this viewpoint, it seems useful to perform a local investigation on the hydrothermal characteristics and to predict the local Nu within the exchanger. The changes in the dimensionless local Nusselt number ($Nu_x/Nu_0$) were computed for the top and bottom duct walls (Figure 13). The lowest values of Nu are observed at the base of the T-obstacle, while its highest amount is reached at the baffle tip. The change in Nu is significantly affected by increasing Re. The most considerable rates of thermal transfer are obtained with high Re, which results from the intensified mixing of fluid particles through the formation of recirculation cells and the interaction with the walls of the T-baffles and the channel. The T-baffles with intense flow rates yield negative turbulent speeds and intensify the fluid agitation, which improves the thermal exchange rates.

From a thermal viewpoint, the investigation of the impact of Re on the dimensionless average Nusselt number ($Nu/Nu_0$) is needed. From the results provided in Figure 14. where Re changes from 12,000 to 32,000, a proportional relationship between the augmentation of $Nu/Nu_0$ and that of Re is shown. The maximum amount of thermal transfer rates is reached on the upper wall due to the highest temperature gradients in this area.

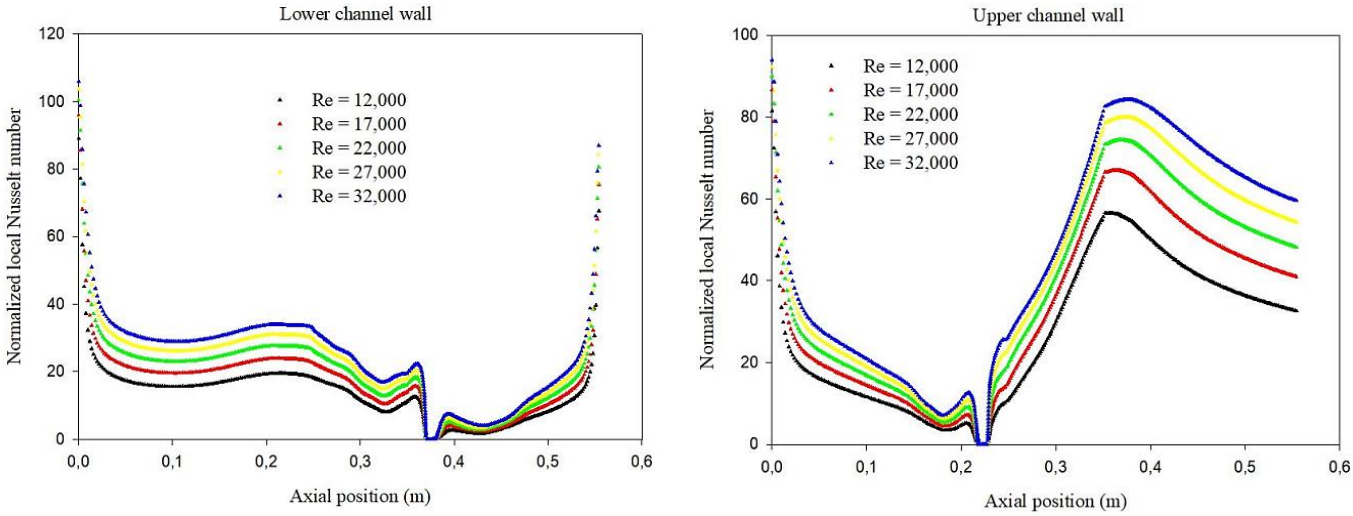


**Figure 13.** Dimensionless local Nusselt number vs. Re. at the (**a**) lower; and (**b**) upper surfaces of the exchanger.

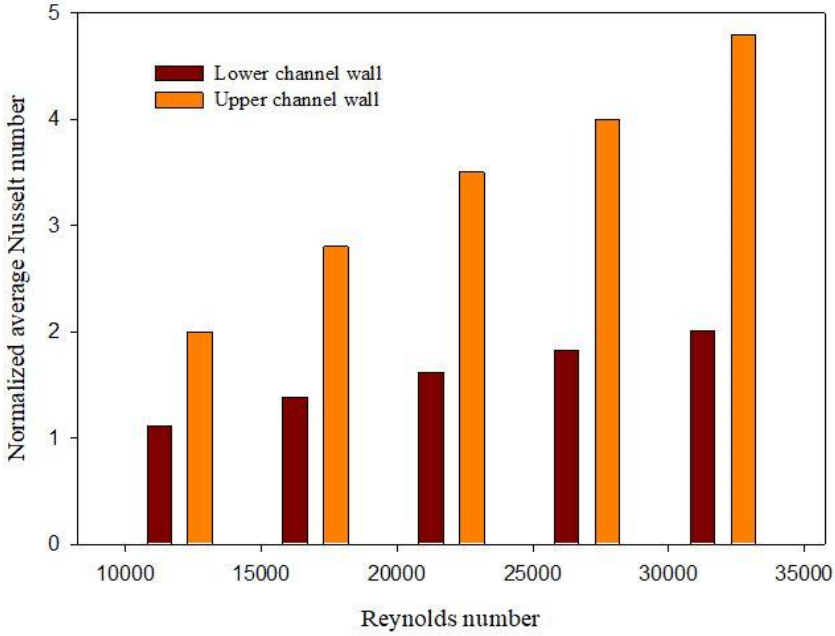


**Figure 14.** Dimensionless average Nusselt number vs. Re.

The change in the dimensionless local skin friction coefficient ($C_f/f_0$) is also inspected along the lower wall (Figure 15a). In the space between 0.1 and 0.3 m, an increase $C_f/f_0$ is shown due to the direction of the streamlines through the 1st VG towards the lower half of the exchanger with intensified speeds. However, $C_f/f_0$ is negligible at the channel exit due to changes in the streamlines that are generated by the 2nd VG.

The values of $C_f/f_0$ along the lower wall of the duct are given in Figure 15b. Weak amounts of $C_f/f_0$ are remarked in the upstream space of the 1st T-baffle. However, $C_f/f_0$ augments in the space between baffles, which results from an abrupt variation in the streamlines. Moreover, the highest amounts of $C_f/f_0$ are shown in the unbaffled zone closed to the channel exit. These significant amounts correspond to the considerable pressure losses that are yielded by the abrupt change in the airflows at the level of the 2nd baffle.

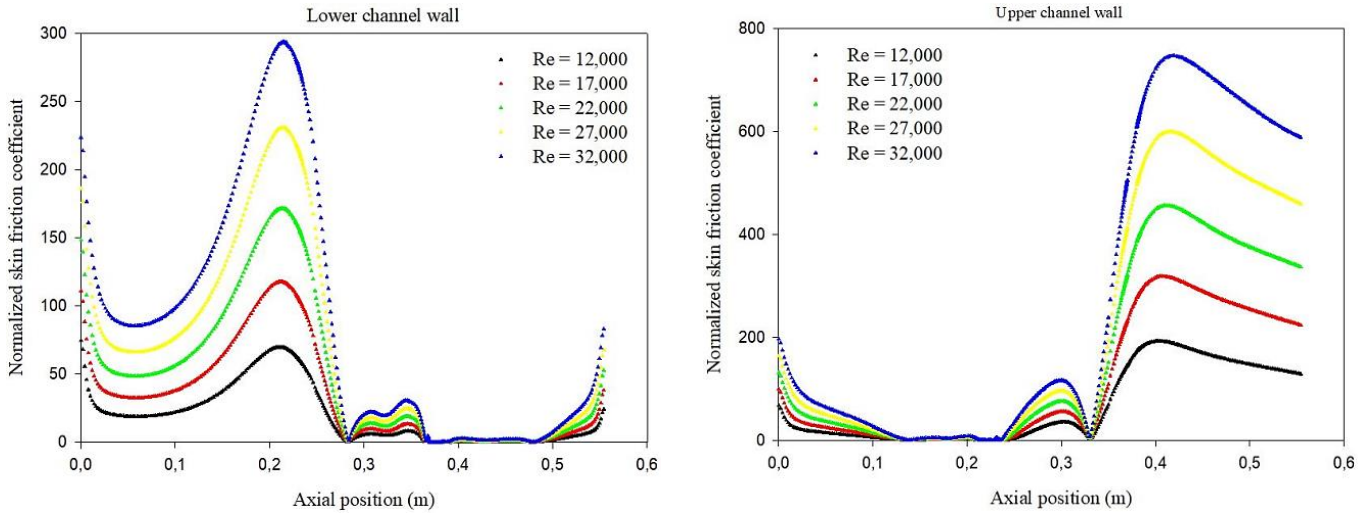


**Figure 15.** Changes in the dimensionless average skin friction coefficient on (**a**) lower; and (**b**) upper surfaces of the exchanger.

Concerning the Reynolds number, the increased Re yields a considerable augmentation of $f/f_0$, as well as the pressure drop. These findings are confirmed by the maps of Figure 16, where the dimensionless average skin friction coefficient ($f/f_0$) is presented at the vertical locations y = 0.073 m and y = −0.073 m and nn obvious relationship between the raise of Re and that of $f/f_0$. The most significant value of $f/f_0$ is remarked on the upper surface of the thermal device due to the highest speed gradients in this area.

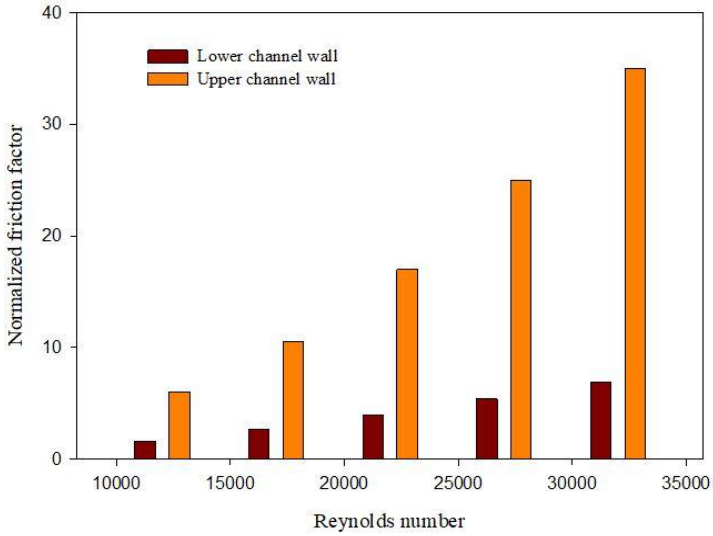


**Figure 16.** Dimensionless friction factor along with the exchanger vs. Re.

In terms of performance, and according to Figure 17, the thermal enhancement factor (TEF) is shown for all tested Reynolds values. Obviously, the performance improvement increases with the higher Reynolds values. All TEF values exceed 1.00. Therefore, having T-shaped VGs can enhance turbulent heat transfer for all flow rates used. The TEF factor reached 1.10 at the lowest value of Re, i.e., 12,000, while it increased to 1.47 with an increase in the flow rate (Re) to 32,000.

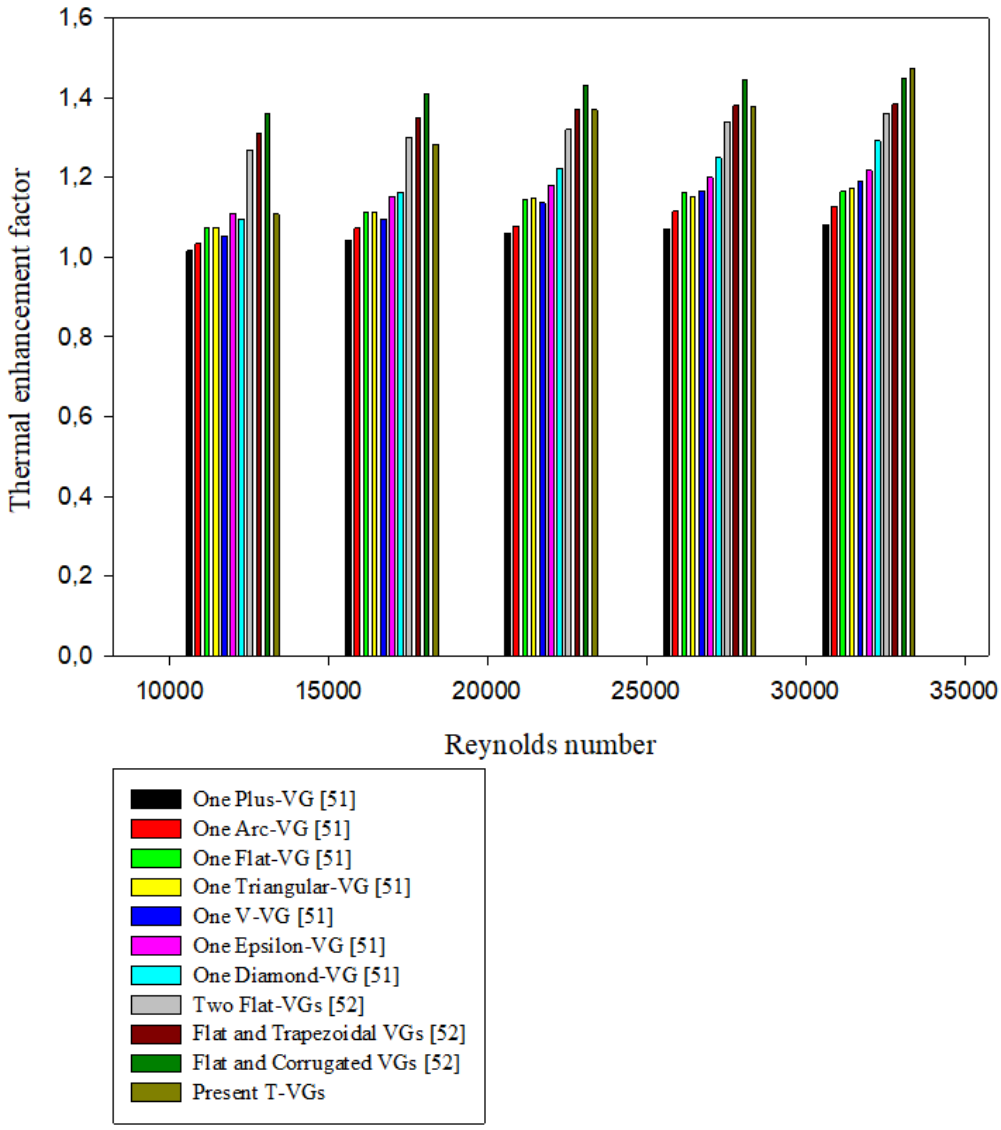


**Figure 17.** Thermal improvement factor vs. Re.

In addition, as shown in Figure 17, the achieved performance is compared to that of several previous studies [51,52]. As the Reynolds number rises, the thermal improvement factor tends to rise as well. For all Re numbers, these improvement factors are larger than unity; they vary between 1.08 and 1.47 depending on the geometrical shapes of the VGs, i.e., CHE with one deflector [51] or two VGs [52] and the flow rate (Re, 12,000 to 32,000). Among all the VGs used, the best improvement factor was obtained with the new tested obstacles, T-shaped VGs. However, this enhancement was slightly lower in the case of two flat-corrugated VGs.

It is important to note that the T-VG model, for a Re number of 32,000, gave a higher improvement factor than that of a case with one VG (Plus, arc, flat, triangular, V, epsilon, and diamond-shaped); or two VGs (flat-flat, flat-trapezoidal, and flat-corrugated-shaped) of about 26.65%, 23.53%, 21.01%, 20.33%, 19.17%, 17.35%, and 12.33%; or 7.75%, 6.05%, and 1.84%, respectively.

Therefore, the T-VG model can be chosen as the best geometric model for good improvement of heat transfer inside a CHE.

## 6. Conclusions

Hydrothermal behavior within a T-baffled CHE was presented. The presence of T-baffles yielded big changes in the flow patterns and thermal fields. The main flow was deflected towards the lower half of the thermal device at the level of the first baffle. In the downstream region of each T-obstacle, a strong recirculation cell was observed.

This estimation showed the following points:

(1) At the VG level, the wall effect is augmented due to the reduction of the passage area of flows, which is estimated here to be 55%, resulting thus in a considerable resistance to the movement of fluid particles.
(2) The 2nd T-shaped VG generates a considerable movement of the fluid particles in the vertical direction, which increases the reattachment length of the separated flows.
(3) The thermal distribution is highly dependent on the flow structures within the CHE. Since the fluid agitation yields an enhanced mixing, it allows thus an excellent heat transfer. The heat transfer process starts just after the 1st VG. Furthermore, and compared with the unbaffled CHE, high amounts of the temperature are observed in the recirculation cells that are formed in the area downstream of the T-VGs. In this recirculation region, a poor heat transfer process is occurring.
(4) The most considerable rates of thermal transfer are obtained with high Re, which results from the intensified mixing of fluid particles through the formation of recirculation cells and the interaction with the walls of the T-baffles and the channel.
(5) The T-baffles with intense flow rates yield negative turbulent speeds and intensify the fluid agitation, which improves the thermal exchange rates.
(6) The highest amounts of $C_f/f_0$ are shown in the unbaffled zone closed to the channel exit. These significant amounts correspond to the considerable pressure losses that are yielded by the abrupt change in the airflows at the level of the 2nd baffle.
(7) The most significant values of Nu and f are observed on the upper surface of the exchanger, due to the highest temperature and speed gradients in this area.
(8) The achieved performance has been compared to that of several previous studies. Among all the VGs reported and investigated, the best improvement factor is obtained with the new tested obstacles, i.e., T-shaped VGs.

As a result, the T-VG model may be selected as the most effective geometric model for improving heat transport within a CHE.

**Author Contributions:** Conceptualization, D.M.M. and H.A. (Houari Ameur); methodology, R.R. and M.I.; software, H.A. (Hijaz Ahmad) and Y.M.; validation, G.L.; formal analysis, D.M.M. and R.R.; investigation, H.A. (Houari Ameur) and M.I.; resources, H.A. (Hijaz Ahmad) and G.L.; data curation, D.M.M.; Funding, F.S.B. and M.A.; writing-original draft preparation, Y.M. and H.A. (Houari Ameur); writing-review and editing, Y.M., H.A. (Hijaz Ahmad) and G.L. All authors have read and agreed to the published version of the manuscript.

**Funding:** Researchers Supporting Project number (TURSP-2020/164), Taif University, Taif, Saudi Arabia.

**Institutional Review Board Statement:** Institutional Review Board Statement and approval number is not applicable.

**Informed Consent Statement:** No informed consent statement is required for this study.

**Data Availability Statement:** All data is available in manuscript.

**Acknowledgments:** Researchers Supporting Project number (TURSP-2020/164), Taif University, Taif, Saudi Arabia.

**Conflicts of Interest:** The authors declare no conflict of interest.

## References


1. Zhang, L.; Cui, X.; Lu, Z.; Miao, C.Y.; Jui, L.W. A novel spiral channel with the growing waviness on the sidewalls for compact high-efficiency heat exchanger. *Appl. Energy* **2021**, *299*, 117332. [CrossRef]
2. Xu, Y.; Cui, G.; Han, X.; Xiao, Y.; Zhang, G. Optimization route arrangement: New concept to achieve high efficiency and quality in heat exchanger network synthesis. *Int. J. Heat Mass Transf.* **2021**, *178*, 121622. [CrossRef]
3. Ahmad, H.; Sakhri, N.; Menni, Y.; Omri, M.; Ameur, H. Experimental study of the efficiency of earth-to-air heat exchangers: Effect of the presence of external fans. *Case Stud. Therm. Eng.* **2021**, *28*, 101461. [CrossRef]
4. Menni, Y.; Azzi, A.; Chamkha, A.J. Enhancement of convective heat transfer in smooth air channels with wall-mounted obstacles in the flow path. *J. Therm. Anal. Calorim.* **2019**, *135*, 1951–1976. [CrossRef]
5. Awais, M.; Bhuiyan, A.A. Heat transfer enhancement using different types of vortex generators (VGs): A review on experimental and numerical activities. *Therm. Sci. Eng. Prog.* **2018**, *5*, 524–545. [CrossRef]
6. Menni, Y.; Azzi, A.; Chamkha, A. A review of solar energy collectors: Models and applications. *J. Appl. Comput. Mech.* **2018**, *4*, 375–401.
7. Chen, D.; Zhang, R.; Cao, X.; Chen, L.; Fan, X. Numerical investigation on performance improvement of latent heat exchanger with sextant helical baffles. *Int. J. Heat Mass Transf.* **2021**, *178*, 121606. [CrossRef]
8. Cao, X.; Zhang, R.; Chen, D.; Chen, L.; Du, T.; Yu, H. Performance investigation and multi-objective optimization of helical baffle heat exchangers based on thermodynamic and economic analyses. *Int. J. Heat Mass Transf.* **2021**, *176*, 121489. [CrossRef]
9. Salhi, J.E.; Zarrouk, T.; Salhi, N. Numerical study of the thermo-energy of a tubular heat exchanger with longitudinal baffles. *Mater. Today Proc.* **2021**, *45*, 7306–7313. [CrossRef]
10. Patankar, S.V.; Liu, C.H.; Sparrow, E.M. Fully developed flow and heat transfer in ducts having streamwise-periodic variations of cross-sectional area. *ASME J. Heat Transf.* **1977**, *99*, 180–186. [CrossRef]
11. Kelkar, K.M.; Patankar, S.V. Numerical prediction of flow and heat transfer in a parallel plate channel with staggered fins. *ASME J. Heat Transf.* **1987**, *109*, 25–30. [CrossRef]
12. Bazdidi-Tehrani, F.; Naderi-Abadi, M. Numerical Analysis of Laminar Heat Transfer in Entrance Region of a Horizontal Channel with Transverse fins. *Int. Commun. Heat Mass Transf.* **2004**, *31*, 211–220. [CrossRef]
13. Tsay, Y.L.; Chang, T.S.; Cheng, J.C. Heat transfer enhancement of backward-facing step flow in a channel by using baffle installed on the channel wall. *Acta Mech.* **2005**, *174*, 63–76. [CrossRef]
14. Pirouz, M.M.; Farhadi, M.; Sedighi, K.; Nemati, H.; Fattahi, E. Lattice Boltzmann simulation of conjugate heat transfer in a rectangular channel with wall-mounted obstacles. *Sci. Iran.* **2011**, *8*, 213–221. [CrossRef]
15. Siddiqui, M.H.K. Heat transfer augmentation in a heat exchanger tube using a baffle. *Int. J. Heat Fluid Flow* **2007**, *28*, 318–328.
16. Demartini, L.C.; Vielmo, H.A.; Möller, S.V. Numeric and experimental analysis of the turbulent flow through a channel with baffle plates. *J. Braz. Soc. Mech. Sci. Eng.* **2004**, *26*, 153–159. [CrossRef]
17. Gajusingh, S.T.; Shaikh, N.; Siddiqui, K. Influence of a rectangular baffle on the downstream flow structure. *Exp. Therm. Fluid Sci.* **2010**, *34*, 590–602. [CrossRef]
18. Sakhri, N.; Draoui, B.; Menni, Y. Experimental study of earth to air heat exchanger performance in arid region. First step: In-situ measurement of ground vertical temperature profile for different depths. *J. Adv. Res. Fluid Mech. Therm. Sci.* **2019**, *56*, 183–194.
19. Sakhri, N.; Moussaoui, A.; Menni, Y.; Sadeghzadeh, M.; Ahmadi, M.H. New passive thermal comfort system using three renewable energies: Wind catcher, solar chimney and earth to air heat exchanger integrated to real-scale test room in arid region (experimental study). *Int. J. Energy Res.* **2021**, *45*, 2177–2194. [CrossRef]
20. Sakhri, N.; Menni, Y.; Chamkha, A.J. Heating capacity of an earth to air heat exchanger in arid regions—Experimental investigation. *J. Appl. Comput. Mech.* **2021**. [CrossRef]
21. Chamkha, A.J.; Menni, Y. Hydrogen flow over a detached v-shaped rib in a rectangular channel. *Math. Model. Eng. Probl.* **2020**, *7*, 178–186. [CrossRef]
22. Boursas, A.; Salmi, M.; Lorenzini, G.; Ahmad, H.; Menni, Y.; Fridja, D. Enhanced heat transfer by oil/multi-walled carbon nano-tubes nanofluid. *Ann. Chim.-Sci. Matériaux* **2021**, *45*, 93–103. [CrossRef]
23. Chekchek, B.; Salmi, M.; Boursas, A.; Lorenzini, G.; Ahmad, H.; Menni, Y.; Ameur, H.; Merrah, M.; Fridja, D. Experimental study of the efficiency of a solar water heater construction from recycled plastic bottles. *Int. J. Des. Nat. Ecodynamics* **2021**, *16*, 121–126. [CrossRef]
24. Hadidi, N.; Rebhi, R.; Bennacer, R.; Menni, Y.; Ameur, H.; Lorenzini, G.; Gepreel, K.A.; Ahmad, H. Thermosolutal natural convection across an inclined square enclosure partially filled with a porous medium. *Results Phys.* **2021**, *21*, 103821. [CrossRef]
25. Menni, Y.; Ameur, H.; Yao, S.W.; Amraoui, M.A.; Inc, M.; Lorenzini, G.; Ahmad, H. Computational fluid dynamic simulations and heat transfer characteristic comparisons of various arc-baffled channels. *Open Phys.* **2021**, *19*, 51–60. [CrossRef]
26. Salmi, M.; Boursas, A.; Mederreg, D.; Lorenzini, G.; Ahmad, H.; Menni, Y.; Ameur, H.; Maoudj, R. Improved heat transfer in w-baffled air-heat exchangers with upper-inlet and lower-exit. *Math. Model. Eng. Probl.* **2021**, *8*, 1–9. [CrossRef]
27. Dutta, P.; Hossain, A. Internal cooling augmentation in rectangular channel using two inclined baffles. *Int. J. Heat Fluid Flow* **2005**, *26*, 223–232. [CrossRef]
28. Sahel, D.; Ameur, H.; Benzeguir, R.; Kamla, Y. Enhancement of heat transfer in a rectangular channel with perforated baffles. *Appl. Therm. Eng.* **2016**, *101*, 156–164. [CrossRef]

29. Yang, Y.T.; Hwang, C.Z. Calculation of turbulent flow and heat transfer in a porous-baffled channel. *Int. J. Heat Mass Transf.* **2003**, *46*, 771–780. [CrossRef]
30. Yilmaz, M. The effect of inlet flow baffles on heat transfer. *Int. Commun. Heat Mass Transf.* **2003**, *30*, 1169–1178. [CrossRef]
31. Guerroudj, N.; Kahalerras, H. Mixed convection in a channel provided with heated porous blocks of various shapes. *Energy Convers. Manag.* **2010**, *51*, 505–517. [CrossRef]
32. Sripattanapipat, S.; Promvonge, P. Numerical analysis of laminar heat transfer in a channel with diamond-shaped baffles. *Int. Commun. Heat Mass Transf.* **2009**, *36*, 32–38. [CrossRef]
33. Zhang, J.F.; He, Y.L.; Tao, W.Q. 3D numerical simulation on shell-and-tube heat exchangers with middle-overlapped helical baffles and continuous baffles—Part I: Numerical model and results of whole heat exchanger with middle-overlapped helical baffles. *Int. J. Heat Mass Transf.* **2009**, *52*, 5371–5380. [CrossRef]
34. Nanan, K.; Thianpong, C.; Pimsarn, M.; Chuwattanakul, V.; Eiamsaard, S. Flow and thermal mechanisms in a heat exchanger tube inserted with twisted cross-baffle turbulators. *Appl. Therm. Eng.* **2017**, *114*, 130–147. [CrossRef]
35. Bekele, A.; Mishra, M.; Dutta, S. Effects of delta-shaped obstacles on the thermal performance of solar air heater. *Adv. Mech. Eng.* **2011**, *3*, 103502. [CrossRef]
36. Zhou, G.; Ye, Q. Experimental investigations of thermal and flow characteristics of curved trapezoidal winglet type vortex generators. *Appl. Therm. Eng.* **2012**, *37*, 241–248. [CrossRef]
37. Menni, Y.; Chamkha, A.J.; Zidani, C.; Benyoucef, B. Study of air flow around flat and arc-shaped baffles in shell-and-tube heat exchangers. *Math. Model. Eng. Probl.* **2019**, *6*, 77–84. [CrossRef]
38. Dong, C.; Zhou, X.F.; Dong, R.; Zheng, Y.Q.; Chen, Y.P.; Hu, G.L.; Xu, Y.S.; Zhang, Z.G.; Guo, W.W. An analysis of performance on trisection helical baffles heat exchangers with diverse inclination angles and baffle structures. *Chem. Eng. Res. Des.* **2017**, *121*, 421–430. [CrossRef]
39. Skullong, S.; Thianpong, C.; Jayranaiwachira, N.; Promvonge, P. Experimental and numerical heat transfer investigation in turbulent square-duct flow through oblique horseshoe baffles. *Chem. Eng. Process. Process. Intensif.* **2016**, *99*, 58–71. [CrossRef]
40. Bopche, S.B.; Tandale, M.S. Experimental investigations on heat transfer and frictional characteristics of a turbulator roughened solar air heater duct. *Int. J. Heat Mass Transf.* **2009**, *52*, 2834–2848. [CrossRef]
41. Menni, Y.; Chamkha, A.J.; Zidani, C.; Benyoucef, B. Baffle orientation and geometry effects on turbulent heat transfer of a constant property incompressible fluid flow inside a rectangular channel. *Int. J. Numer. Methods Heat Fluid Flow* **2020**, *30*, 3027–3052. [CrossRef]
42. Menni, Y.; Azzi, A.; Chamkha, A.J.; Harmand, S. Effect of wall-mounted V-baffle position in a turbulent flow through a channel: Analysis of best configuration for optimal heat transfer. *Int. J. Numer. Methods Heat Fluid Flow* **2019**, *29*, 3908–3937. [CrossRef]
43. Chamoli, S.; Thakur, N.S. Correlations for solar air heater duct with V-shaped perforated baffles as roughness elements on absorber plate. *Int. J. Sustain. Energy* **2016**, *35*, 1–20. [CrossRef]
44. Jedsadaratanachai, W.; Boonloi, A. Effects of blockage ratio and pitch ratio on thermal performance in a square channel with 30° double V-baffles. *Case Stud. Therm. Eng.* **2014**, *4*, 118–128. [CrossRef]
45. Kumar, A.; Bhagoria, J.L.; Sarviya, R.M. Heat transfer and friction correlations for artificially roughened solar air heater duct with discrete W-shaped ribs. *Energy Convers. Manag.* **2009**, *50*, 2106–2117. [CrossRef]
46. Sriromreun, P.; Thianpong, C.; Promvonge, P. Experimental and numerical study on heat transfer enhancement in a channel with Z-shaped baffles. *Int. Commun. Heat Mass Transf.* **2012**, *39*, 945–952. [CrossRef]
47. Petukhov, B.S. Heat transfer and friction in turbulent pipe flow with variable physical properties. *Adv. Heat Transf.* **1970**, *6*, 503–564.
48. Dittus, F.W.; Boelter, L.M.K. Heat transfer in automobile radiators of the tubular type. *Int. Commun. Heat Mass Transf.* **1985**, *12*, 3–22. [CrossRef]
49. Patankar, S.V. *Numerical Heat Transfer and Fluid Flow*; McGraw-Hill: New York, NY, USA, 1980.
50. Leonard, B.P.; Mokhtari, S. *Ultra-Sharp Nonoscillatory Convection Schemes for High-Speed Steady Multidimensional Flow. NASA TM 1-2568*; NASA Lewis Research Center: Cleveland, OH, USA, 1990.
51. Menni, Y.; Azzi, A.; Chamkha, A.J. Modeling and analysis of solar air channels with attachments of different shapes. *Int. J. Numer. Methods Heat Fluid Flow* **2019**, *29*, 1815–1845. [CrossRef]
52. Menni, Y.; Azzi, A. Design and performance evaluation of air solar channels with diverse baffle structures. *Comput. Therm. Sci.* **2018**, *10*, 225–249. [CrossRef]